FULL PAPER

Wireless Microfluidic Systems for Programmed, Functional Transformation of Transient Electronic Devices

Chi Hwan Lee, Seung-Kyun Kang, Giovanni A. Salvatore, Yinji Ma, Bong Hoon Kim, Yu Jiang, Jae Soon Kim, Lingqing Yan, Dae Seung Wie, Anthony Banks, Soong Ju Oh, Xue Feng, Yonggang Huang, Gerhard Troester, and John A. Rogers*

Electronic systems that enable programmable transformation of functional behaviors by remote control or by autonomous responses to user-defined circumstances create unusual engineering opportunities, where physical changes in the hardware induce desired changes in operation. This paper presents materials and device architectures for technologies of this type, in which localized microfluidic chemical etching of targeted constituent components in the electronics occurs in a sequential, selective manner. Custom circuits that include reconfigurable radio-powered thermal actuators with analog amplifiers and square waveform generators illustrate the concepts.

1. Introduction

Electronic systems that provide reliable, high-performance operation in platforms that include water-soluble, nontoxic materials are of growing interest in temporary biomedical implants, resorbable environmental monitors, disposable devices, hardware-secure digital memories, and other applications that are not well served by conventional technologies.[1] Such types of systems represent a subset of a broader class of a technology referred to as transient electronics. Early work[2] examined sequentially dissolvable electronics in which variations in the thicknesses and types of the constituent materials determine a time sequence for dissolution across the areas of integrated devices. An important recent advance[3] in this field followed from the realization of on-demand, triggered dissolution via a remotely controlled microfluidic system. In the present paper, we demonstrate that these platforms can be extended for use in multistaged transformations of functional behaviors in the transient electronics by means of programmed microfluidic chemical etching at

Dr. C. H. Lee, Dr. S.-K. Kang, Dr. G. A. Salvatore,
Dr. B. H. Kim, D. S. Wie, A. Banks
Department of Materials Science and Engineering
and Frederick Seitz Materials Research Laboratory
University of Illinois at Urbana-Champaign
Urbana, IL 61801, USA

Dr. G. A. Salvatore
Electronics Laboratory
Swiss Federal Institute of Technology
Zurich 8092, Switzerland

Dr. Y. Ma, Dr. Y. Jiang, Prof. Y. Huang
Department of Civil and Environmental Engineering
and Mechanical Engineer
Center for Engineering and Health and Skin Disease Research Center
Northwestern University
Evanston, IL 60208, USA

J. S. Kim
Department of Chemistry
University of Illinois at Urbana-Champaign
Urbana, IL 61801, USA

L. Yan
Department of Chemical and Biomolecular Engineering
University of Illinois at Urbana-Champaign
Urbana, IL 61801, USA

Prof. S. J. Oh
Department of Materials Science and Engineering
University of Illinois at Urbana-Champaign
Urbana, IL 61801, USA

Prof. S. J. Oh
Department of Materials Science and Engineering
Korea University
Seoul 136-713, Republic of Korea

Prof. X. Feng
Department of Engineering Mechanics
Center for Mechanics and Materials
Tsinghua University
Beijing 100084, China

Prof. X. Feng
Laboratory of Nano-Optoelectronics
Institute of Semiconductors
Chinese Academy of Sciences
Beijing 100083, China

Prof. G. Troester
Electronics Laboratory
Swiss Federal Institute of Technology
Zurich 8092, Switzerland

Prof. J. A. Rogers
Department of Materials Science and Engineering
Chemistry, Mechanical Science, and Engineering
Electrical, and Computer Engineering
Beckman Institute for Advanced Science and Technology
and Frederick Seitz Materials, Research Laboratory
University of Illinois at Urbana-Champaign
Urbana, IL 61801, USA
E-mail: jrogers@illinois.edu

www.MaterialsViews.com

ADVANCED
FUNCTIONAL
MATERIALS
www.afm-journal.de

FULL PAPER

selective, strategic locations. Several examples, including programmable radio frequency (RF), analog and digital circuits for communication and data encryption, demonstrate the utility of these platforms.

2. Results and Discussion

Figure 1a presents the structure of a wireless microfluidic device for on-demand, functional transformation of transient electronics. The design includes: 1) microfabricated thermal actuators, 2) thermally expandable polymers, 3) fluid reservoirs, and 4) microfluidic channels, all on a supporting substrate that can be integrated with transient electronic systems. The thermal actuators consist of serpentine traces of Au (300 nm thick) formed on an FR4 substrate (≈1 mm thick). Micromachined features of relief in a slab of cyclic olefin polymer (COP) define circular reservoirs and microfluidic channels upon sealing against the FR4 using a double-sided adhesive film (ARclear, Adhesive Research). Conformal layers of parylene (5 μm thick) and Al (3 μm thick) can be deposited onto the relief features to improve the chemical resistance and reduce leakage.[4] A layer of thermally expandable polymer (300 μm thick, Expancel 031 DU 40, AkzoNobel) lies between this cap and the FR4, in the regions of the reservoirs. This material undergoes an irreversible change in volume (increase to ≈5 times of its original volume) when heated to temperatures >80 °C, to an extent that it nearly completely fills the reservoir regions. Fine powders of materials such as sodium hydroxide (NaOH, 99.99%, Sigma-Aldrich), embedded in the serpentine microfluidic channels form highly corrosive etchants when mixed with water upon its ejection from the reservoirs.[3] The resulting etchants emerge at the outlet ports and onto targeted locations of the transient electronics, where they selectively eliminate key constituent materials (i.e., Al). Details associated with the materials and fabrication procedures appear in the Experimental Section.

Figure 1b presents the wireless control hardware, including a four-channel RF receiver and transmitter (SKU108447, operating current: 10 mA at 12 V, transmitting frequency: 315 MHz, transmitting distance: ≈200 m in open areas, Banggood Inc.) and a power relay module, for independent control of each thermal actuator. Figure 1c (top column) presents thermal maps collected with an infrared (IR) camera (FLIR SC650, Wilsonville, OR) during sequential, wireless activation of each actuator in the array. Joule heating induced by passage of current from a power source (Agilent 6200B DC power supply, ≈600 mW) leads to peak temperatures of ≈90 °C within 10 s after the wireless triggering using a remote control unit. The observations agree with finite element analysis (FEA) of the coupled thermal responses (Figure 1c, bottom column). Figure 1d shows an example of the sequential, triggered release of water with red, green, purple, and orange dyes. Another demonstration, as in Figure 1e, involves a configuration of microfluidic channels that releases the dyed water into a single location. The graph in Figure 1f shows experimental (IR thermal monitor) and computational (FEA) results of the average temperatures of the powered actuator (marked A; ≈90 °C) and adjacent actuator (marked B, C, and D; ≈room temperature) in Figure 1c.

For envisioned applications, the ability to avoid fluid leakage or evaporation represents a key requirement. Figure 1g presents results showing that the systems described here are capable of retaining water in the reservoirs with an approximate evaporation rate of ≈0.39 mg d^{-1} by exploiting a sealing layer of Al (3 μm thick, water vapor permeability: <0.2 g mm m^{-2} d^{-1}) along with an additional conformal layer of parylene (5 μm thick, water vapor permeability: <0.1 g mm m^{-2} d^{-1}) to further improve the chemical resistance and reduce the permeability of water/vapor through the inner walls of reservoirs and microfluidic channels.[4] Optical images of the components coated with these sealing layers are in Figure S1 (Supporting Information).

The microfluidic system can operate via different modes of triggering, not only by user-activated schemes, but also by autonomous responses to time signals or environmental changes (i.e., light, humidity). **Figure 2**a presents a schematic diagram of trigger modules that include internal clocks (1/16 DIN, eight-pin octal base), photodetectors (LDR, 12 V light-emitting diodes, light control photoresistor with relay modules), and humidity sensors (DC 5 V, 3–5 s, soil humidity actuation mode relay modules), where activation occurs based on a preset time, light exposure intensity and ambient humidity, respectively. The relays are powered at 20 V to provide the current for the thermal actuators. The graphs in Figure 2b–d present experimental results (IR measurements) for the temperature as a function of time shortly before and after activation. In each case, the temperature quickly rises to ≈90 °C as the thermal actuator remains active for ≈10 s, followed by a decrease upon deactivation. The insets provide optical images of the trigger modules. It is noteworthy that these design strategies are general to other types of trigger modules, such as chemical sensors.

This type of device can be integrated with transient electronic systems that exploit a combination of transient and standard components, including integrated circuits, radios, microelectromechanical systems, sensors, and others.[2] The example shown in **Figure 3**a exploits an RF antenna (Au traces, 800 nm thick) and a resistive heating element (Au traces, 100 nm thick), as a simple, radio-powered thermal actuator. The antenna includes segments constructed with transient materials (Mg, 2 μm thick; Al, 1 μm thick). This entire structure is integrated with the wireless microfluidic device for triggered release of solutions (water and an aqueous solution of NaOH) to dissolve the metals (Mg and Al, respectively) in a time-sequential, selective way. Each material gradually dissolves in a manner defined by the etching rates (1.2 nm min^{-1} for Mg and 30 nm min^{-1} for Al by water and NaOH, respectively),[3,5] which shifts the resonant frequency of the antenna by changing its effective length. Figure 3b shows the normalized temperature profiles associated with operation at frequencies adjusted to maximize the level of heating for three stages: the initial circuit (stage 0), after dissolution of Mg (stage 1) and after dissolution of Mg and Al (stage 2). These frequencies, which shift from 1.81 GHz (stage 0, black) to 1.90 GHz (stage 1, red) and 2.10 GHz (stage 2, blue) due to reduction in the length of the antenna by dissolution of the Mg and Al segments, provide the highest energy-conversion efficiency (ECE), as defined by impedance matching.[2] Figure 3c shows the changes in the maximum ECE frequency and the maximum temperature during the triggered transformation

ADVANCED
FUNCTIONAL
MATERIALS
www.afm-journal.de

Materials
Views
www.MaterialsViews.com
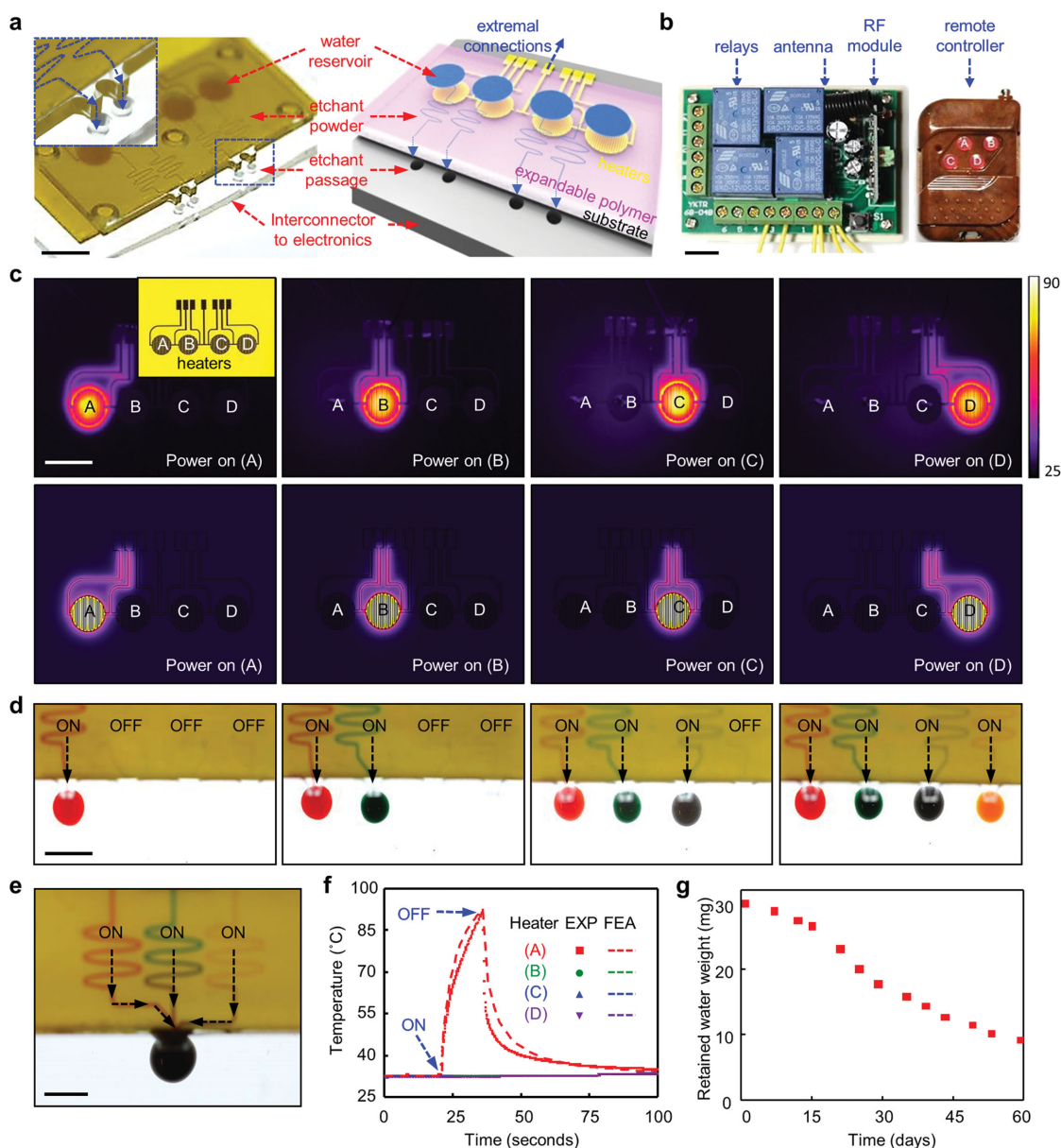
Figure 1. Layout of a wirelessly controlled microfluidic device and characterization of the integrated thermal actuators that serve as pumps. a) Optical image (left, scale bar, 5 mm) and schematic illustration (right) of the device, which consists of four independent microfluidic channels in a sealing cap, a thermally expandable polymer, and microfabricated thermal actuators made of Au (≈300 nm thick) on an FR4 substrate. Fine chemical powders can be filled in the serpentine regions of the microfluidic channels. b) Optical images (scale bar, 1 cm) of a four-channel radio frequency (RF) wireless system (left) and a remote control unit (right). c) Infrared (IR) images (top, scale bar, 1 cm) and corresponding FEA results (bottom) of the distributions of temperature for sequential operation of the thermal actuators (marked A, B, C, and D). The inset shows a magnified optical image of the actuators. d) Optical images (scale bar, 5 mm) of the sequential, triggered release of water with red, green, purple, and orange dye from the microfluidic channels. e) Optical image (scale bar, 2 mm) of the triggered release of water with red, green, and orange dye from the device onto a single location. f) Experimental and computational (FEA) results of the average temperatures of the thermal actuators (marked A, B, C, and D in Figure 1c). The temperature of the activated element (marked A) reaches at ≈90 °C while the others (marked B, C, and D) remain at room temperature. g) Measured weights of the retained water in the reservoirs coated with sealing layers of Al (3 μm thick) and parylene (5 μm thick) for 60 d.

process. The IR thermal maps in Figure 3d show that the maximum temperature decreases as a result of shifts in the ECE frequency and associated loss of impedance matching at a fixed frequency of 1.81 GHz (optimum value for stage 0), where the power and distance are 50 W and 6 cm, respectively.

The example in Figure 3e exploits a planar Au inductor with transient interconnects, addressable by sequential release of solutions at a single location. The optical images in Figure 3e (right) show that the triggered release of water and NaOH solution allow programmed dissolution of the Mg and Al segments,

www.MaterialsViews.com

ADVANCED
FUNCTIONAL
MATERIALS
www.afm-journal.de

FULL PAPER
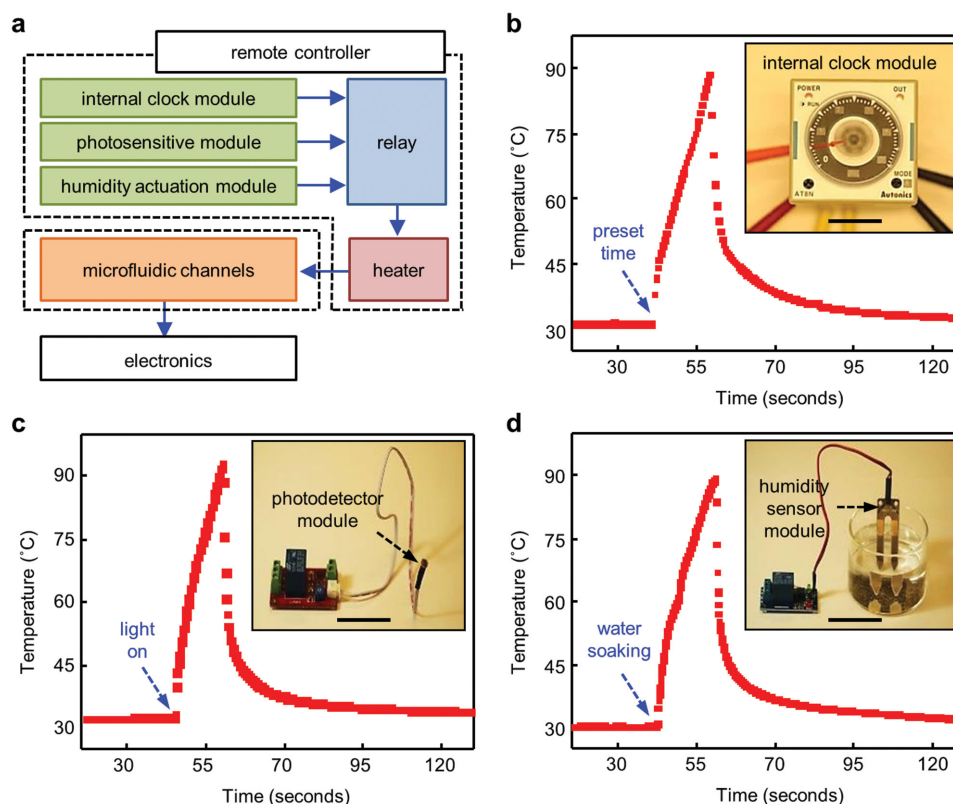
Figure 2. Modes for autonomous triggering and characterization of thermal actuators. a) Schematic diagram of various triggering modes based on a time delay relay, a photodetector, and a hydration sensor. b–d) Experimental and computational (FEA) results of the average temperatures of thermal actuators triggered by each module. The insets (scale bar, 2, 7, and 7 cm, respectively) show optical images of the trigger modules.

respectively, in a sequential and selective manner (water dissolves the Mg but not the Al). The corresponding shifts of resonance frequencies (black, stage 0, 233 MHz; red, stage 1, 222 MHz; and blue, stage 2, 173 MHz) appear in Figure 3f,g. These changes result from the alteration of pathways of current through the crossing lines, with a shift toward lower frequencies as the number of turns in the coil turns increases due to etching of the crossing lines.[2]

Other applications involve reconfigurable circuits for signal processing and data encryption. **Figure 4** shows an example of such concepts implemented with custom circuits, including analog amplifiers and square waveform generators, whose gain and oscillation frequency, respectively, can be tuned by the selective dissolution of Mg and Al resistors/interconnects. The devices combine circuits built on a four-layer printed circuit board and a microfluidic system like those described previously (Figure 4a). A layer of polydimethylsiloxane (Sylgard 184, Dow Corning) with predefined holes inserted in between these two components directs the flow of liquids to the circuit board (magnified view in Figure 4a, right). As before, the transient components consist of Mg (300 nm thick) and Al (500 nm thick) traces, dissolvable in water and aqueous NaOH solution, respectively. Optical images of the analog amplifier and square wave generator appear in Figure S2 (Supporting Information). Here, triggered transience allows tuning of the output gain and resonant frequency for the analog amplifier and waveform generator, respectively, by selective etching of

the Mg and/or Al. Figure 4b presents a series of microscope images collected before and after the elimination of Al. The times for complete dissolution of the Al (500 nm thick) and Mg (300 nm thick) elements are ≈10 and ≈110 min, respectively. Figure 4c shows a schematic illustration of the amplifier; the configuration used here provides a gain defined by the ratio of the feedback and input resistances. Two of each Al and Mg traces (represented as $R_i(t)$ where $i = 1, 2, 3, 4$ in the schematic) connect in series with each of the four input resistances. The initial voltage gain of the circuit is 4 ($R = R_0 = 22$ kΩ); this value can be shifted to 3, 2, and 1 via selective change in $R_i(t)$ (Figure 4d).

The square waveform generator consists of a Schmidt trigger with Al and Mg traces in series with four capacitors (Figure 4e). The value of the feedback resistance and the overall capacitance set the frequency. As a result, the frequency can adopt several different, discrete values depending on the number of the capacitors that connect to ground. For this experiment, R_0 is 10 kΩ, R is 22 kΩ, and C is 10 nF. These values result in an initial oscillating frequency of 1.1 kHz (Figure 4f). The selective dissolution of the wires causes the frequency to shift to 1.5 kHz after the dissolution of the first wire, 2.2 kHz after the second, and 4.4 kHz when only one capacitor is connected. In addition to these steady-state values, the transient behavior of the gain and oscillating frequency change during the dissolution process. Figure S3 (Supporting Information) shows the experimental results. As discussed in the Experimental Section,
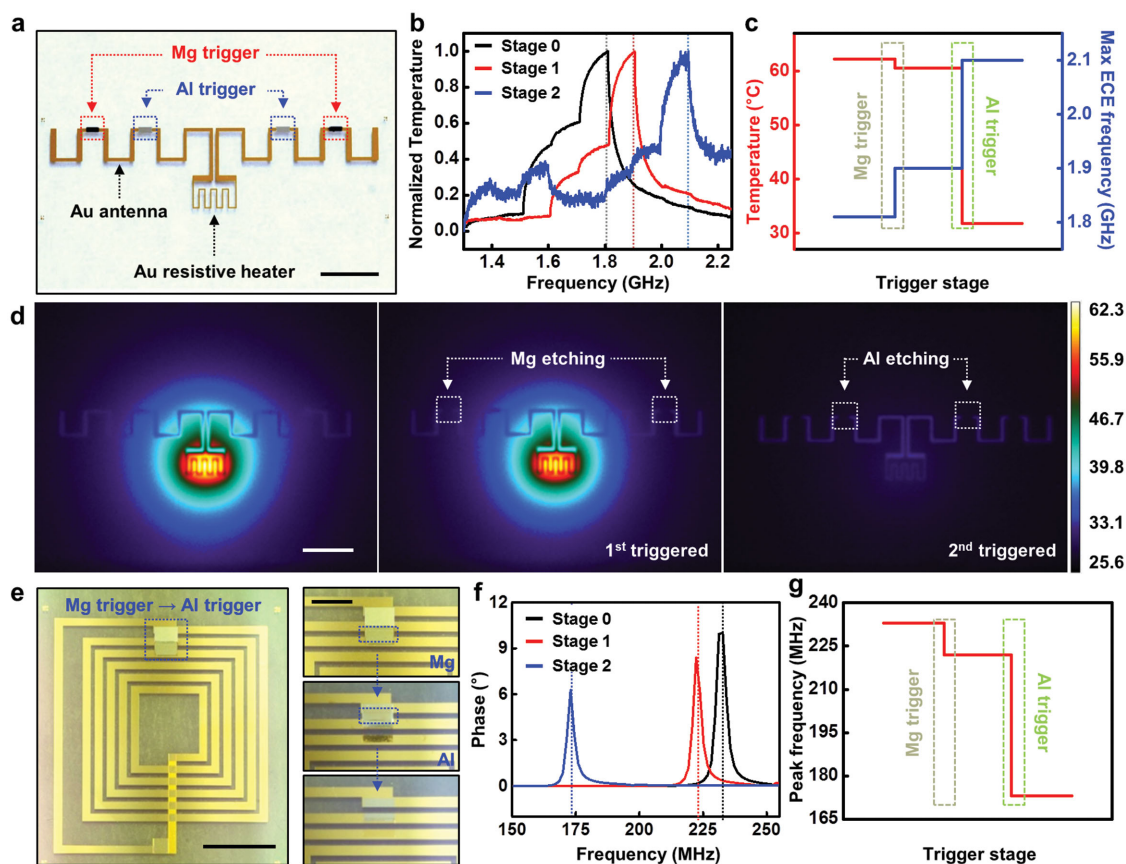
Figure 3. Triggered functional transformation in transient radio frequency (RF) devices. a) Optical image (scale bar, 5 mm) of an antenna (Au, 800 nm thick) and a serpentine thermal actuator (Au, 100 nm thick) with transient segments of Al (1 μm thick, blue) and Mg (2 μm thick, red). b) Variation of the normalized temperature of the thermal actuator during exposure to RF at different frequencies. The temperature is normalized by the maximum temperature of each circuit. The frequency and maximum temperature of maximum energy-conversion efficiency (ECE) are 1.81 GHz and 62.3 °C, 1.90 GHz and 60.6 °C, and 2.10 GHz and 31.8 °C, respectively. The maximum ECE frequency shifts toward higher values upon dissolution of Al and Mg. c) Changes in maximum ECE frequency and peak temperatures (evaluated at 1.81 GHz) at different stages of transformation. d) IR images (scale bar, 5 mm) of the system at different stages, captured during exposure to RF at a fixed frequency of 1.81 GHz (initial maximum ECE frequency). e) Inductor (left, scale bar, 5 mm) designed to transform via dissolution of Mg and Al traces that act as electrical shorts in a planar spiral coil. Magnified views (scale bar, 2 mm) of the crossover lines at several stages during triggered transformation (top, stage 0; middle, stage 1; and bottom, stage 2). f) Changes in the phase response at these different stages (black, stage 0; red, stage 1; and blue, stage 2). The resonance frequency shifts toward lower frequency upon dissolution of the Al and Mg. g) Changes in resonance frequency as a function of time during triggered transformation.

the circuits are designed to operate in steady state; however, a time-controlled dissolution process together with feedback or accurate electrical modeling offers an opportunity to exploit nonlinear effects, of potential relevance for applications in data encryption, for instance.
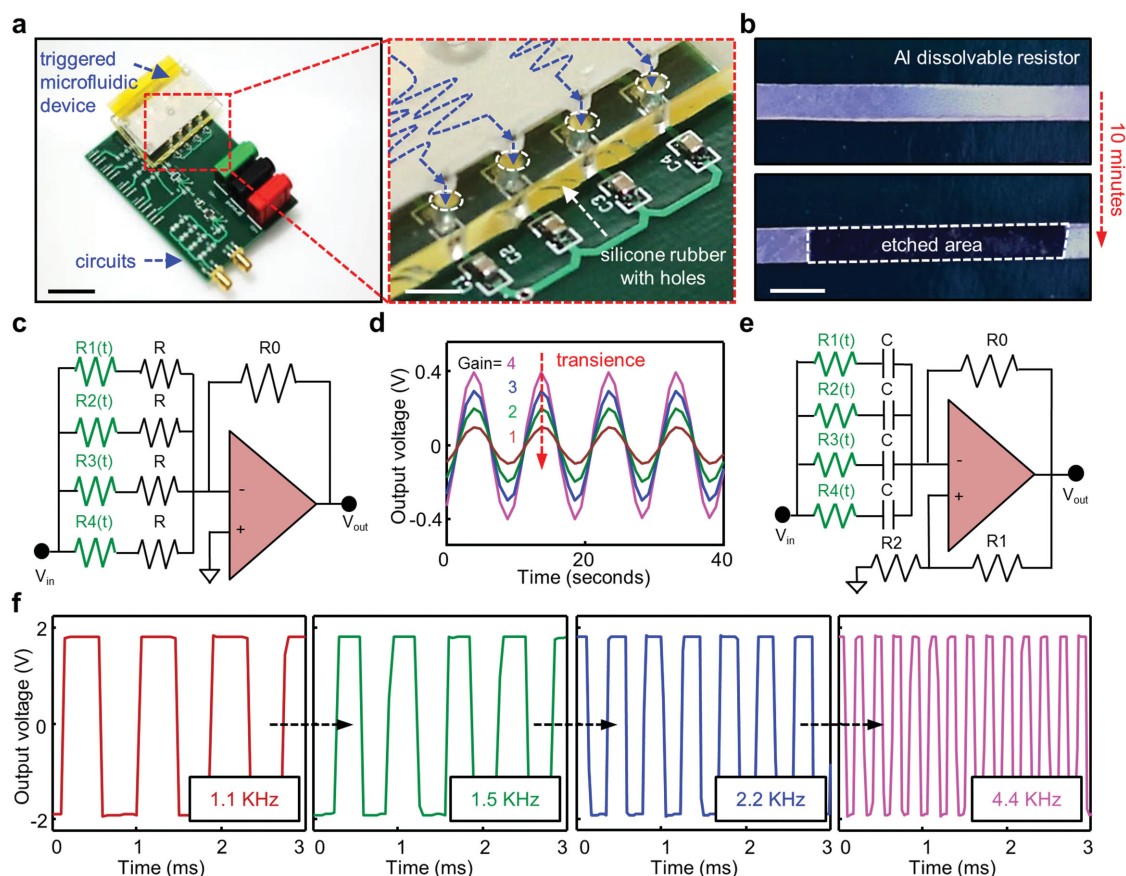
from photonics to optoelectronics and microelectromechanical systems.

4. Experimental Section

Fabrication of Microfluidic Device for Triggered Transformation: Photolithographic patterning of a layer of Au (300 nm thick) formed by electron beam evaporation yielded heater elements on an FR4 substrate (400 μm thick, ePlastics). A layer of thermally expandable polymer (300 μm thick; Expancel 031 DU 40, AkzoNobel) composed of a mixture of polydimethylsiloxane (Sylgard 184, Dow Corning) and thermally expandable polymer at a ratio of 2:1 by weight, was spin-cast and cured in a convection oven at 70 °C for 4–6 h. Mechanical milling defined relief structures on a substrate of COP (2 mm thick, Zeon Chemicals). Deposition of a conformal layer of parylene (5 μm thick) and Al (3 μm thick) formed a secondary seal to improve the chemical resistance and reduce permeability of water/vapor through the inner walls of reservoirs and microfluidic channels. Filling these features with finely ground chemical powders and bonding the resulting substrate onto the fully

3. Conclusion

To summarize, the concepts introduced here allow on-demand, functional transformation in transient electronics via selective, sequential dissolution of targeted constituent materials via a microfluidic device activated with various modes of triggering inputs. These capabilities provide great versatility in designs and potential applications of transient electronics. Demonstration examples shown here exploit reconfigurable circuits for signal processing and data encryption, and suggest possibilities for use in other kinds of advanced technologies, ranging

Figure 4. Triggered functional transformations in signal processing devices. a) Optical image (scale bar, 1 cm) of an integrated system, including a signal processing circuit and a wireless microfluidic device. An enlarged image (right, scale bar, 5 mm) shows the bonding interface between these components. b) Optical image (scale bar, 1 mm) of a dissolvable interconnect (Al, 500 nm thick) before (top) and after (bottom) the triggered release of an etching solution (aqueous NaOH). c) Schematic illustration of a circuit design for an analog amplifier. The green color denotes the dissolvable resistors. d) Changes in output gain of the amplifier by sequential elimination of each resistor. e) Schematic illustration of the circuit design for the waveform generator. The green color denotes the dissolvable resistors. f) Changes in resonant frequency of the waveform generator induced by sequential elimination of each resistor.

cured expandable polymer layer using a double-sided adhesive film (ARclear, Adhesive Research) yielded sealed microfluidic channels. We note that sodium hydroxide (NaOH) is hygroscopic and a glove box is needed for preventing air-slake during the process. Distilled water was injected by a syringe into reservoirs through the predefined holes (0.5 mm diameter). Sealing the holes and outlet with copper foil (300 nm thick) to prevent evaporation of water completed the fabrication.

Fabrication and Electrical Characterizations of Antennas and Inductors: Photolithographic patterning of a layer of Au formed by electron beam evaporation yielded antennas (800 nm thick) and serpentine resistors (100 nm thick) on a glass substrate with an adhesive layer of Cr (1 nm thick). Electron beam evaporation formed films for the metal segments of Al (1 μm thick) and Mg (2 μm thick). The spiral induction coils used Au (800 nm thick) and SiN$_x$ (600 nm thick) deposited by an electron beam evaporator and a plasma enhanced chemical vapor deposition, respectively. Crossover transient resistors/interconnectors consisted of Mg (2 μm thick) and Al (1 μm thick). Measurements defined the RF characteristics of antennas and inductors after the triggered release of etching solutions (water and NaOH) from reservoirs onto target locations. The RF absorption determined the change in temperature measured by an IR camera (FLIR SC650, Wilsonville, OR). The distance and power were 6 cm and 50 W, respectively. The frequency to yield the maximum temperature defined the ECE. With a frequency fixed to

the optimal value for the initial circuit, the triggered dissolution of the transient interconnectors caused sharp decreases in temperature, due to the shifts in the ECE. Coupling the inductor to a circular primary coil (1.6 cm diameter) in the near field yielded the sample resonance frequency through an impedance analyzer.[6]

Fabrication of Custom Signal Processing Systems with Dissolvable Interconnectors: The analog amplifier and square waveform generator exploited a printed circuit board as a substrate. Deposition of Al (500 nm thick) and Mg (300 nm thick) by electron beam evaporation on a Kapton strip (60 μm thick) defined the dissolvable interconnects bonded to the circuits with a conductive silver epoxy. A bias of 2 V and input signal of 100 mV were applied to the analog amplifier. An oscilloscope captured the output signals for all cases.

Modeling of the Transient Behavior of Gain and Oscillating Frequency: A simple analysis of the analog amplifier enabled first-order modeling of the gain for each dissolution step ($R_0 = R$ in Figure 4d):

$$A(t) = -\frac{3R_1(t) + 4R}{R_1(t) + R} \quad \text{for } R_2(t) = R_3(t) = R_4(t) = 0$$
$$\text{(dissolution of the first wire)} \tag{1}$$

$$A(t) = -\frac{2R_2(t) + 3R}{R_2(t) + R} \quad \text{for } R_1(t) = \infty, \ R_3(t) = R_4(t) = 0$$
$$\text{(dissolution of the second wire)} \tag{2}$$

$$A(t) = -\frac{R_3(t) + 2R}{R_3(t) + R} \quad \text{for } R_1(t) = R_2(t) = \infty, R_4(t) = 0 \quad (3)$$
$$\text{(dissolution of the third wire)}$$

$$A(t) = -\frac{R}{R_4(t) + R} \quad \text{for } R_1(t) = R_2(t) = R_3(t) = \infty \quad (4)$$
$$\text{(dissolution of the fourth wire)}$$

The transient analysis for the oscillator relied on frequency-dependent behavior of the capacitors and the digital/unstable nature of the circuit. A schematic for the case of the dissolution of the first wire (i.e., $R_2(t) = R_3(t) = R_4(t) = 0$), where $C_1 = C_2 = C_3 = C_4$, appears in Figure S4 (Supporting Information). During the transition of V_{out}, the capacitors behaved as short circuits. Hence, when the voltage across $R_1(t)$ equals to V_x, the oscillator became unstable. This behavior was particularly prominent for dissolution of the fourth wire. The system returned to a stable state as $R_1(t)$ approached infinity (complete dissolution). In the configuration, this instability occurred when $R_1(t) = R_0 = 10$ kΩ.

Finite Element Analysis: A commercial software (ABAQUS)[7] package was used to study the thermal response of the thermal actuators. The heaters (copper, 300 nm thick, thermal conductivity: 400 W m^{-1} K^{-1}, density: 8900 kg m^{-3}, specific heat: 390 J K^{-1} kg^{-1}) were modeled by the heat transfer shell element (DS4), while the substrates (FR4, 400 μm thick, thermal conductivity: 0.3 W m^{-1} K^{-1}, density: 1750 kg m^{-3}, specific heat: 1200 J K^{-1} kg^{-1}),[8] thermally expandable polymer (300 μm thick, thermal conductivity: 0.24 W m^{-1} K^{-1}, density: 970 kg m^{-3}, specific heat: 1460 J K^{-1} kg^{-1}, measured by experiment), and COP (2 mm thick, thermal conductivity: 0.135 W m^{-1} K^{-1}, density: 1020 kg m^{-3}, specific heat: 1000 J K^{-1} kg^{-1})[9] were modeled by the heat transfer brick element (DC3D8).

Supporting Information

Supporting Information is available from the Wiley Online Library or from the author.

[1] H. Tao, S.-W. Hwang, B. Marelli, B. An, J. E. Moreau, M. Yang, M. A. Brenckle, S. Kim, D. L. Kaplan, J. A. Rogers, F. G. Omenetto, *Proc. Natl. Acad. Sci. U.S.A.* **2014**, *111*, 17385.

[2] S.-W. Hwang, S.-K. Kang, X. Huang, M. A. Brenckle, F. G. Omenetto, J. A. Rogers, *Adv. Mater.* **2015**, *27*, 47.

[3] C. H. Lee, J.-W. Jeong, Y. Liu, Y. Zhang, Y. Shi, S.-K. Kang, J. Kim, J. S. Kim, N. Y. Lee, B. H. Kim, K.-I. Jang, L. Yin, M. K. Kim, A. Banks, U. Paik, Y. Huang, J. A. Rogers, *Adv. Funct. Mater.* **2015**, *25*, 1338.

[4] T.-N. Chen, D.-S. Wuu, C.-C. Wu, C.-C. Chiang, Y.-P. Chen, R.-H. Horng, *Plasma Proc. Polym.* **2007**, *4*, 180.

[5] L. Yin, H. Cheng, S. Mao, R. Haasch, Y. Liu, X. Xie, S.-W. Hwang, H. Jain, S.-K. Kang, Y. Su, R. Li, Y. Huang, J. A. Rogers, *Adv. Funct. Mater.* **2014**, *24*, 645.

[6] X. Huang, Y. Liu, H. Cheng, W.-J. Shin, J. A. Fan, Z. Liu, C.-J. Lu, G.-W. Kong, K. Chen, D. Patnaik, S.-H. Lee, S. Hage-Ali, Y. Huang, J. A. Rogers, *Adv. Funct. Mater.* **2014**, *24*, 3846.

[7] ABAQUS Analysis User's Manual, V6.10, ABAQUS Inc., Johnston, RI, USA **2010**.

[8] Y. Ding, J.-K. Kim, *Microelectron. Reliab.* **2008**, *48*, 149.

[9] C.-S. Park, K. Namkoong, Y.-S. Lee, J.-W. Rhee, *US Patent US20090074623 A1*, **2009**.